Aeroacoustic study of a wavy stator leading edge in a realistic fan/OGV stage

Casalino, Damiano; Avallone, Francesco; Gonzalez-Martino, Ignacio; Ragni, Daniele

DOI
10.1016/j.jsv.2018.10.057

Publication date
2019

Document Version
Final published version

Published in
Journal of Sound and Vibration

Citation (APA)
Casalino, D., Avallone, F., Gonzalez-Martino, I., & Ragni, D. (2019). Aeroacoustic study of a wavy stator leading edge in a realistic fan/OGV stage. *Journal of Sound and Vibration*, *442*, 138-154. https://doi.org/10.1016/j.jsv.2018.10.057

Journal of Sound and Vibration 442 (2019) 138–154

Contents lists available at ScienceDirect

Journal of Sound and Vibration

journal homepage: www.elsevier.com/locate/jsvi

Aeroacoustic study of a wavy stator leading edge in a realistic fan/OGV stage

Damiano Casalino [a,b,*], Francesco Avallone [a], Ignacio Gonzalez-Martino [c], Daniele Ragni [a]

[a] Delft University of Technology, Kluyvenweg 1, 2629 HS, Delft, Netherlands
[b] Exa Corp., Curiestrasse 4, 70563, Stuttgart, Germany
[c] Exa Corp., Les Collines de l'Arche, 76 Route de la Demi-Lune, 92057, Paris la Défense Cedex, France

ARTICLE INFO

Article history:
Received 28 March 2018
Revised 11 August 2018
Accepted 29 October 2018
Available online 5 November 2018

Keywords:
Fan noise
Wavy leading edge
Source diagnostic test

ABSTRACT

The effect of sinusoidal serrations applied to the leading-edge of the vanes of a realistic fan stage is investigated using high-fidelity numerical simulations. The CFD solver PowerFLOW based on a hybrid lattice-Boltzmann/very-large-eddy-simulation model is used to compute the unsteady flow and radiated noise of the 22-in source diagnostic test fan rig of the NASA Glenn Research Center. A computational model validated for three different geometries of the outlet guide vanes with straight leading edge is used. A subset of validation results is reported to prove the capability of the solver to accurately predict the influence of the stator geometry on the far-field noise. Different sinusoidal leading edge serrations are investigated for a radial and a swept stator and the same rotor and operating conditions. The influence of the serrations on the acoustic far-field and noise power level is reported in relation to the statistical properties of the velocity fluctuations in the wake of the rotor. Some noise reductions are obtained when the undulation amplitude and wavelength are large enough compared to the integral scales of the impinging turbulence fluctuations.

1. Introduction

Current turbofan design trends towards large bypass ratio engines (up to 12–13), dictated by the necessity of reducing the fuel consumption without increasing the engine weight, result in axially compact engines [1], with a smaller distance between the rotor and the Outlet Guide Vane (OGV). As a consequence, the tonal contribution of the rotor/stator interaction noise is expected to increase for three reasons: (i) the wake from the rotor blades is deeper and thinner closer to the rotor, thus resulting in larger time derivatives of the OGV loading, (ii) the rotor blades experience unsteady loading due to the periodic flow distortion past the OGV, a potential flow effect that rapidly vanishes as the interstage distance increases, (iii) the noise generated by the OGV is scattered by the rotor and additional cut-on modes are excited. The effect of the interstage distance on the broadband rotor/stator interaction noise is less intuitive, since it depends on the turbulent velocity levels and integral scales in the wake of the rotor, and both quantities undergo a variation in the axial direction due to the development of instabilities in the shear layer of the wake.

One of the passive noise reduction concepts for rotor/stator interaction noise that has recently received the attention of the aeroacoustic community is the wavy leading edge. The effect of a serration is to reduce the correlation in the radial direction by

* Corresponding author. Delft University of Technology, Kluyvenweg 1, 2629 HS, Delft, Netherlands.
E-mail address: D.Casalino@tudelft.nl (D. Casalino).

https://doi.org/10.1016/j.jsv.2018.10.057
0022-460X/

decorrelating the source in adjacent undulation valleys, to create a destructive interference along the serration edge through the generation of vanishing subcritical gust components, or simply to decorrelate the fluctuations induced at the valley and the peak of the undulations. As discussed hereafter, these effects have been experimentally observed and confirmed by Computational Aero-Acoustics (CAA) simulations for wing sections. This serves as motivation for the present numerical investigation carried out on a realistic fan stage configuration.

Inspired by whale flippers, the effects of leading edge serrations on the aerodynamic performances of wing sections have been studied since the Seventies. Soderman [2] performed lift and drag measurements in a closed wind tunnel of an aerofoil with small sharp serrations on the leading-edge. He observed an increase of the incidence of maximum lift and a small drag penalty at low angle of attack. The delayed stall was related to the generation of streamwise vortices at the leading edge that energize the boundary layer through momentum transfer and delay the leading edge flow separation. Further experiments confirmed the effects of serrations on the stall behaviour of wings [3,4] and whale flippers with tubercles [5,6].

Aeroacousticians have been also inspired by nature. In the pioneering work by Graham [7], the silent flight of owl was related with the special adaptations of the feathers in several species. By comparing the wing and the feathers of silently flying owls with the ones of an owl belonging to a species that does not fly silently, he identified three peculiarities that are responsible for the quiet flight: the leading edge comb, the trailing edge fringe and the downy upper surface of the feathers. He also proposed to use similar features for the reduction of aircraft noise, together with lower wing loading and flight speed, as also inspired by owls. Later on, using simple modelling assumptions, Lilley [8] concluded that the feather adaptations of the owl lead to a major noise reduction above 2 kHz.

Recent works on the use of leading-edge serrations for the reduction of the aerofoil/turbulence interaction noise have focused on the effects of the ratio between the undulation amplitude h_s and the turbulence length scale L_t of the impinging flow, the effect of the serration angle θ_s, and thus the undulation wavelength λ_s. Recent experiments [9] conducted on a flat plate and a NACA-65(12)10 aerofoil of 0.15 m chord and 0.45 m span interacting with grid-induced turbulence in a free stream with velocity U in the range 20–60 m/s, determined the existence of an optimal undulation wavelength $\lambda_s^{\mathrm{opt}} \simeq 4L_t$, corresponding to a condition at which adjacent sources in the undulation valleys are incoherently excited. They finally argued that the noise power level ratio between serrated and straight edge aerofoil at the frequency f is inversely proportional to the Strouhal number $\mathrm{St}_h = fh_s/U$, i.e. the ratio between h_s and the streamwise wavelength U/f, for $\mathrm{St}_h \gtrsim 0.2$ up to the value where serration self-noise starts to dominate.

Several numerical studies for the wavy leading edge have been conducted by using Euler equations with ingested turbulence modelled as a convected harmonic upwash gust [10], a Kraichnan-Fourier superposition of upwash gust components matching the spectral energy content of homogeneous isotropic turbulence [11], and a stochastic three-dimensional divergence-free velocity field also matching the spectral energy content of homogeneous isotropic turbulence [12]. These studies showed that the noise reduction increases when the ratio of the leading edge undulation amplitude to the gust wavelength is increased. Moreover, Clair et al. [11] separated the effects of subcritical and supercritical gust components along the serration edge, as analytically investigated by Roger et al. [13], thus recognising the role of the serration angle and wavelength on the radiated noise. More recently, Gea-Aguilera et al. [14] solved linearized Euler equations past a NACA 0012 aerofoil with stochastic anisotropic turbulence of prescribed levels and integral scales in the streamwise (L_x) and spanwise (L_z) directions. They observed that the maximum decorrelation between noise sources along the leading edge and consequent maximum noise reduction are achieved when $L_x < 2h_s$ (peak-to-valley decorrelation) and $L_z \lesssim \lambda_s/2$ (valley-to-valley decorrelation).

The goal of the present paper is to investigate the benefits associated with a wavy OGV leading edge for a realistic engine geometry and turbulence anisotropy, by performing non-linear compressible flow simulations of a fan stage configuration. An extensively validated numerical model of the 22-in Source Diagnostic Test (SDT) fan rig of the NASA Glenn Research Center [15,16] is used as a reference for a series of simulations performed by using different sinusoidally serrated OGVs. Two reference configurations are considered, a radial stator (baseline) and a swept stator (low-noise). All simulations are performed at approach conditions corresponding to 61.7% of the nominal rotational speed.

The organization of the paper is as follows. Section 1 provides information about the geometry of the problem and details about the wavy leading edge. The flow solver and the computational model are the same as the ones used by Casalino et al. [17] and reported, for the sake of completeness, in Section 2, together with a subset of reference results for the straight OGVs in Section 3. The integral scales of the turbulent fluctuations in the interstage are estimated using the approach presented in Section 4. Results for the wavy OGVs are reported and discussed in Section 5 in relation to the radiated far-field noise and to the integral length scales in the wake of the rotor. Due to the limited number of serration geometries considered, only provisional conclusions for one single operating conditions are given in the conclusion section.

2. Fan stage configurations and sinusoidal leading edge

The reference engine is the SDT fan rig of the NASA Glenn Research Center [15,16], made available by NASA in the framework of the AIAA Fan Broadband Noise (FBN) prediction workshop. The engine model and the wavy OGV are described in this section.

2.1. Reference geometries

Fig. 1 shows three variants of the OGV configurations: a 54-vane *baseline* radial OGV, a 26-vane *low-noise* swept OGV and a 26-vane *low-count* radial OGV. All the other parts, with the exception of very small variations of the inner and outer casing profiles

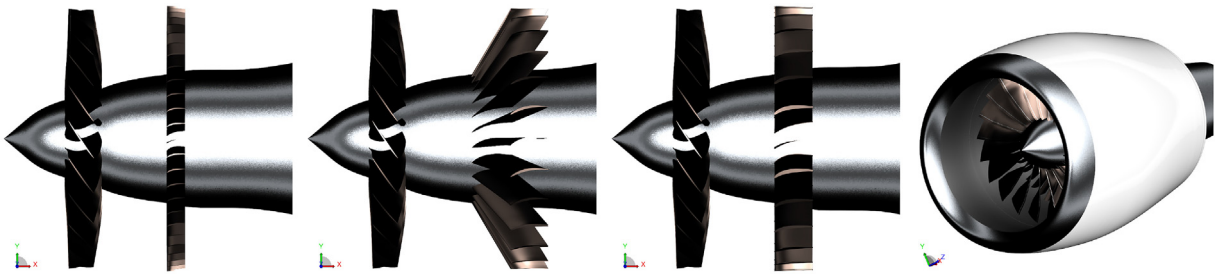

Fig. 1. SDT engine configurations; from left to right, baseline, low-noise, low-count, and nacelle.

Table 1
Wavy OGV design parameters.

Design #	OGV Conf.	λ_s (mm)	$\widetilde{h}_s$	h_s (mm)
1	Low-Noise	7	0.15	1.88
2	Low-Noise	3.5	0.075	0.94
3	Low-Noise	14	0.3	3.76
4	Baseline	14	0.3	1.80
5	Baseline	14	0.6	3.60
6	Baseline	16	0.8	4.80

downstream of the OGV, are the same for the three configurations. The nacelle is perfectly axisymmetric without struts. In order to reproduce the stinger used in the experiment, a cylindrical prolongation of the centerbody has been added to the model released by NASA. The rotor radius is 0.2786 m, the bypass exhaust radius is 0.2710 m and the lip intake radius is 0.2962 m. The rotor is constituted of 22 blades and the casing/blade-tip gap is about 0.5 mm.

2.2. Wavy OGV

The wave leading edge is originated using the following procedure:

- A structured mesh is initially created starting from an imported unstructured surface mesh of a stator blade by individuation of the leading- and trailing-edge lines, defined as a sequence of N_s equally-spaced constant points along the span from a minimal to maximal radial distance, and by construction of the chord line for every radial section.
- For every radial strip j delimited by the grid cuts j and $j+1$, a fixed point $\mathbf{x}_F^j$ is individuated on the chord of length c^j, such that $\left|\mathbf{x}_F^j - \mathbf{x}_{\mathrm{LE}}^j\right| = \sigma c^j$, where $\mathbf{x}_{\mathrm{LE}}^j$ is the local leading-edge point, and σ is a prescribed relative portion of the chord affected by the morphing procedure.
- For every radial strip, the coordinates of the blade points such that $d = \left|\mathbf{x}^j - \mathbf{x}_{\mathrm{LE}}^j\right| / c^j \leq \sigma$ are modified using the following formula:

$$\mathbf{x}_w^j = \mathbf{x}_F^j + \left(\mathbf{x}^j - \mathbf{x}_F^j\right) \left[1 + \cos\left(2\pi r/\lambda_s\right)\right] (1 - d/\sigma)\, \widetilde{h}_s, \tag{1}$$

where r is the radial coordinate of the point, $\widetilde{h}_s = h_s/(\sigma\, c^j)$ is the prescribed undulation amplitude factor, and h_s is the amplitude.

Six different wavy stator designs are considered in the present study, all obtained using the chord ratio $\sigma = 0.15$ and the parameters reported in Table 1. Corresponding images of the stator blades are shown in Fig. 2. The choice of these parameters for designs #1 and #2, was quite arbitrary, whereas for the other ones was based on a priori estimation of the integral scales of the turbulent fluctuations in the interstage volume, as discussed hereafter.

3. Numerical model

The Lattice-Boltzmann (LB) CFD/CAA solver PowerFLOW 5.4a is used to compute the transient flow inside and around the engine. A Ffowcs-Williams and Hawkings (FW-H) approach is then used to extrapolate the near field solution sampled on a permeable surface to the far-field. Exa fan-noise best practice setup is used for all simulations.

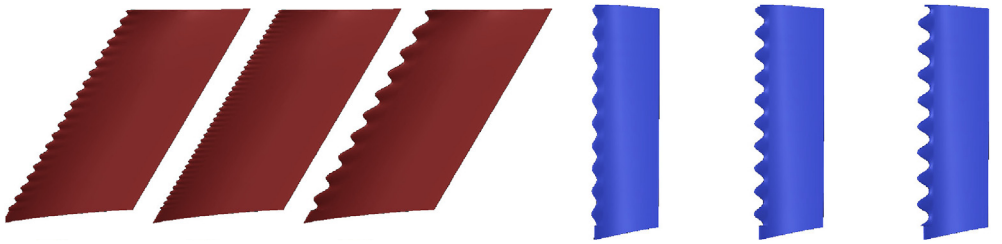

Fig. 2. Wavy OGVs: from left to right, design #1, to #2 and #3 (red), and design #4, #5 and #6 (blue). (For interpretation of the references to color in this figure legend, the reader is referred to the Web version of this article.)

3.1. CFD/CAA computational approach

PowerFLOW solves the Boltzmann equation for the distribution function $f(\mathbf{x}, t, \mathbf{v})$ on a hexahedral mesh automatically generated around bodies, which consist of one or more connected solid parts. The function f represents the probability to find, in the elementary volume d$\mathbf{x}$ around $\mathbf{x}$ and in the infinitesimal time interval $(t, t + \mathrm{d}t)$, a number of fluid particles with velocity in the interval $(\mathbf{v}, \mathbf{v} + \mathrm{d}\mathbf{v})$. The Boltzmann equation is solved by discretizing the particle velocity space into a prescribed number of values, in magnitude and direction. These discrete velocity vectors are such that, in a prescribed time step, one particle is advected from one point of the mesh to 19 neighbouring points, including the point itself, which constitute the computational stencil of the so-called D3Q19 scheme (three-dimensional 19 states model). It can be demonstrated that using 19 particle velocity states ensures sufficient lattice symmetry to recover the Navier-Stokes equations for an isentropic flow [18]. For high subsonic Mach number simulations, e.g, flows with local Mach number greater than 0.5, as in the present case, the LB solver is coupled with the solution of the entropy equation through a Lax-Wendroff finite difference scheme on the Cartesian LB mesh [19]. Once the distribution function is computed, the macroscopic flow quantities, density and linear momentum, are simply determined through discrete integration: $\rho(\mathbf{x}, t) = \sum_j f_j(\mathbf{x}, t)$ and $\rho\mathbf{u}(\mathbf{x}, t) = \sum_j f_j(\mathbf{x}, t)\ \mathbf{v}_j$. All the other quantities are determined through thermodynamic relationships for an ideal gas.

Solving the lattice Boltzmann equation is equivalent to performing a Direct Numerical Simulation (DNS) of the Navier-Stokes equations in the limits of the dynamic range (Mach number) that can be accurately covered by the number of discrete particle velocity vectors, and in the limits of the lattice resolution required to capture the smallest scales of turbulence. For high Reynolds number flows, turbulence modelling is incorporated into the LB scheme by changing the relaxation time in the collision operator that is computed according to a Bhatnagar-Gross-Krook (BGK) approximation [20]. The turbulent kinetic energy and the turbulent dissipation are obtained by solving a variant of the Re-Normalisation Group (RNG) $k - \epsilon$ model for the unresolved scales [21]. This approach is referred to as LB Very Large Eddy Simulation (LB-VLES). Since it is prohibitive to resolve the wall boundary layer using a Cartesian mesh approach down to the viscous sub-layer in high Reynolds number applications, a wall function approach is used to model boundary layers on solid surfaces.

The LB equation is solved on a grid composed of cubic cells. A variable resolution by a factor two is allowed between adjacent regions. Consistently, the time step is varied by a factor two between two adjacent resolution regions. Solid surfaces are automatically facetized within each cell intersecting the wall geometry using planar surface elements. No-slip and slip wall boundary conditions on these elements are imposed using a particle bounce-back process and a specular reflection process, respectively [22]. Extremely complex geometries can be treated automatically.

The far-field noise is computed through an integral extrapolation based on a FW-H acoustic analogy formulation. A forward-time solution [23] based on Farassat's formulation 1A [24] is used. The free-stream convective effects are taken into account directly in the integral formulation [25].

3.2. Computational setup

Images of the computational setup are shown in Fig. 3. The rotor and the spinner are encompassed by a volume (purple) that defines the rotating mesh region. The centerbody is extended with a solid cylinder since, similarly to the experiments, no primary jet is included in the simulation. The green and yellow surfaces in the interstage volume in the top-left image denote regions explored by Hot-Wire (H-W) measurements and are referred to as station # 1 and station # 2, respectively. The second one is at the same axial location as the baseline OGV leading edge, and measurements are therefore available only for the low-noise configuration. The FW-H integration surface consists of three parts: a spherical sector around the intake, a cylindrical connector and a conical surface in the exhaust region. The cone is opened at its downstream extremity in order to avoid contamination of the acoustic signals due to integration of jet shear-layer hydrodynamic fluctuations. The downstream extension of the cone is however sufficient to recover the bypass duct radiation over the angular range of interest. The present setup is identical to the one used by Casalino et al. [17], with the exceptions of the shape of the trip added on the suction side of the rotor blades to trigger the turbulent transition in the wake of the rotor. Instead of a trip with a rectangular section, a zig-zag trip of height linearly varying from 0.3 mm at 5% of the span (root) to 0.1 mm at 95% ot the span, 5 mm wavelength and 1 mm amplitude, located at 10% of the chord, has been used, and all the simulations have been repeated, revealing a slight

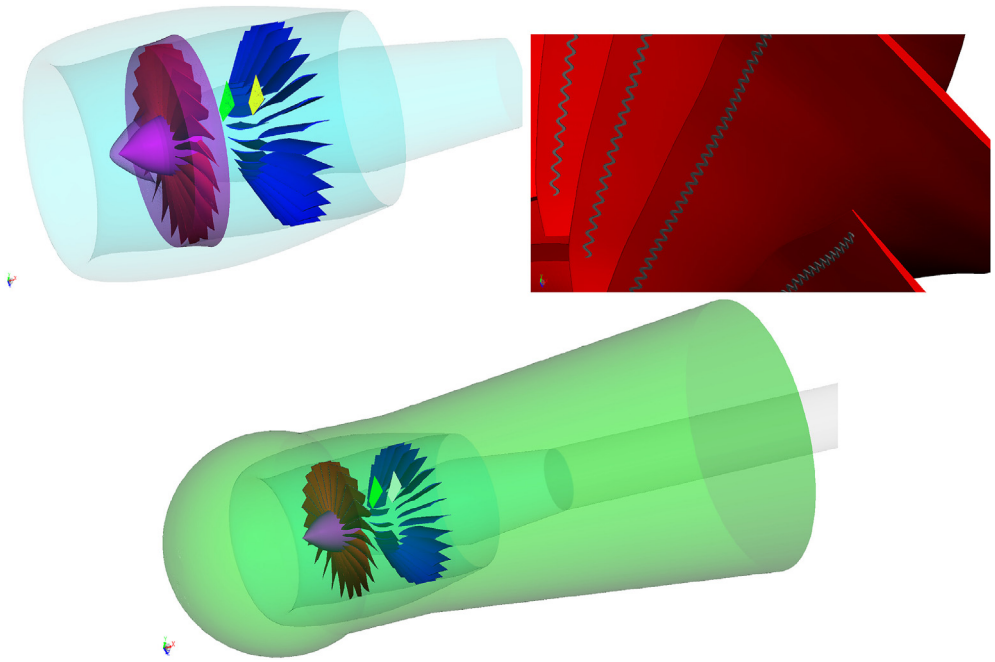

Fig. 3. Computational setup (low-noise OGV) and detail view of the zig-zag trip and FW-H surface.

improvement of the prediction of noise levels at high frequencies. For the sake of consistency, the reference results reported in Section 3 are the new ones obtained using the zig-zag trip.

All simulations reported in this paper have been performed by using, as initial condition, a statistically converged solution obtained with a coarser mesh. Then, the simulations are performed by sampling the solution along 10 rotor revolutions after a very short initial transient of three blade passages. The CPU cost is of the order of six thousand CPU hours per rotor revolution using 720 cores Intel Sandybridge 2.7 GHz.

All the narrow band far-field noise and sound power level spectra have been computed using the Welch's periodogram method, using a signal length of $2.738 \cdot 10^{-1}$ s, a bandwidth of 28.63 Hz, and 13 spectral averages with 43% overlap. The noise signal at each microphone has been obtained by appending four FW-H signals computed at four azimuthal locations (every 90°), and truncated at an integer number of blade passage periods.

4. Reference results

In this section a subset of the available results for the three OGV configurations with straight leading edge are reported and shortly discussed. These results have been presented by Exa during the 4th FBN Prediction Workshop held on June 8th, 2017 in Denver, as a special session of the 23rd AIAA/CEAS Aeroacoustics Conference. Only results for the approach operating condition are reported in this work.

Fig. 4 shows a comparison between measurements and simulation results at station #1 for the baseline configuration. The three components of the phase-locked average velocity, and the corresponding standard-deviation (SDV) values are plotted on an angular sector covering one rotor blade passage. The axial and azimuthal components are Laser Doppler Velocimetry (LDV) measurements, whereas the radial component is Hot Wire (HW) measurement. In Ref. et al. [17], HW measurements have been used for the three velocity components, resulting in an overestimation of the axial component by about 10%. After a discussion with engineers at NASA Glenn, it was argued that HW measurements were affected by a calibration error, and that LDV phase-locked data are more reliable. Unfortunately, LDV measurements are only available for the axial and azimuthal velocity components, say first and third row, respectively. The average field is fairly well predicted, the main discrepancy being an underestimation of the radial velocity component, maybe due to a calibration bias of the H-W measurements. It is worth mentioning that, for all configurations, the mass flow rate is predicted within an error of 1%, whereas the total pressure ratio across the full stage is predicted within an error of 0.4%. The predicted SDV levels are also in fair agreement with the measurements, with two main negative marks: an overestimation of about 20% of the axial and azimuthal velocity fluctuation levels close to the outer wall, and an overestimation of about 10% of the radial velocity fluctuation levels in the half-span region. It is worth mentioning that the predicted SDV fields are also affected by a statistical convergence error, since averages have been performed over 10 rotor revolutions only.

Figs. 5 and 6 show comparisons between measurements and simulation results at stations #1 and #2, respectively, for the low-noise configuration. At station #1 the same trends observed for the baseline configuration can be reported. Indeed, at this

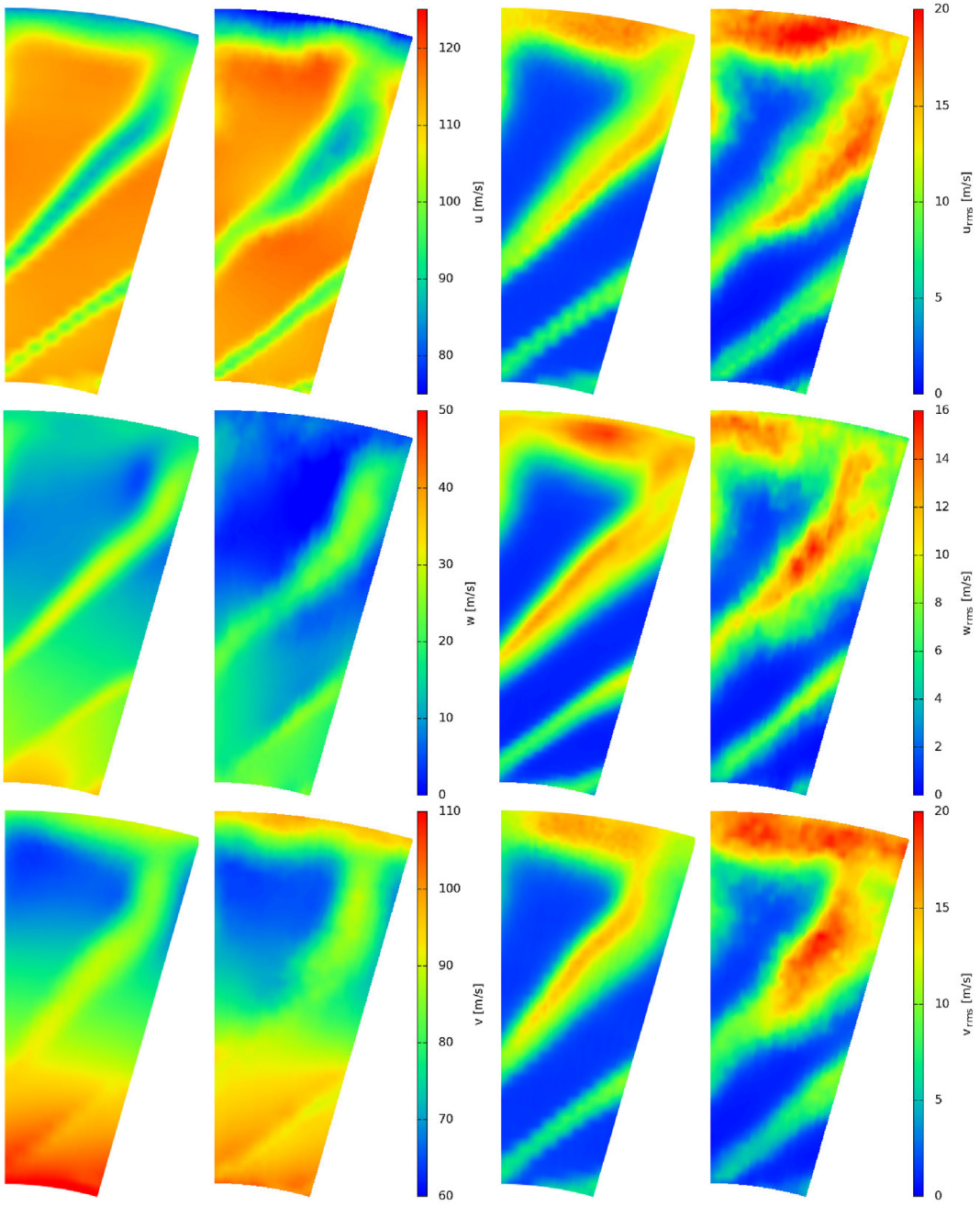

Fig. 4. Phase-locked average (left block) and SDV velocity (right block) at station #1 for the baseline OGV [m/s]. Axial, radial and azimuthal velocity in the top, middle and bottom rows, respectively. Measurements on the left column, simulations on the right.

distance from the OGV, the velocity field is not affected by the OGV geometry in a significant way. At station #2 a fairly good agreement between measurements and predictions can be observed. In particular, the levels are quite well captured by the simulations, as well as the turbulent mixing and spreading of the rotor wake.

The velocity maps at station #2 provide a certain confidence of the capability of the method to predict the correct velocity field upstream of the OGV. This is proven for the low-noise configuration, and reasonably expected for the baseline one, for which no measurements are available at station #2. Therefore, the main discrepancy between measurements an overestimation of about 20% of the azimuthal velocity SDV. The impact of these errors on the predicted far-field noise can be evaluated by considering the formula obtained by Amiet [26] for an isolated aerofoil of chord c and span L at zero incidence in a turbulent stream. The Power Spectral Density (PSD) of the far-field noise in the aerofoil midspan plane, at a distance r from the aerofoil

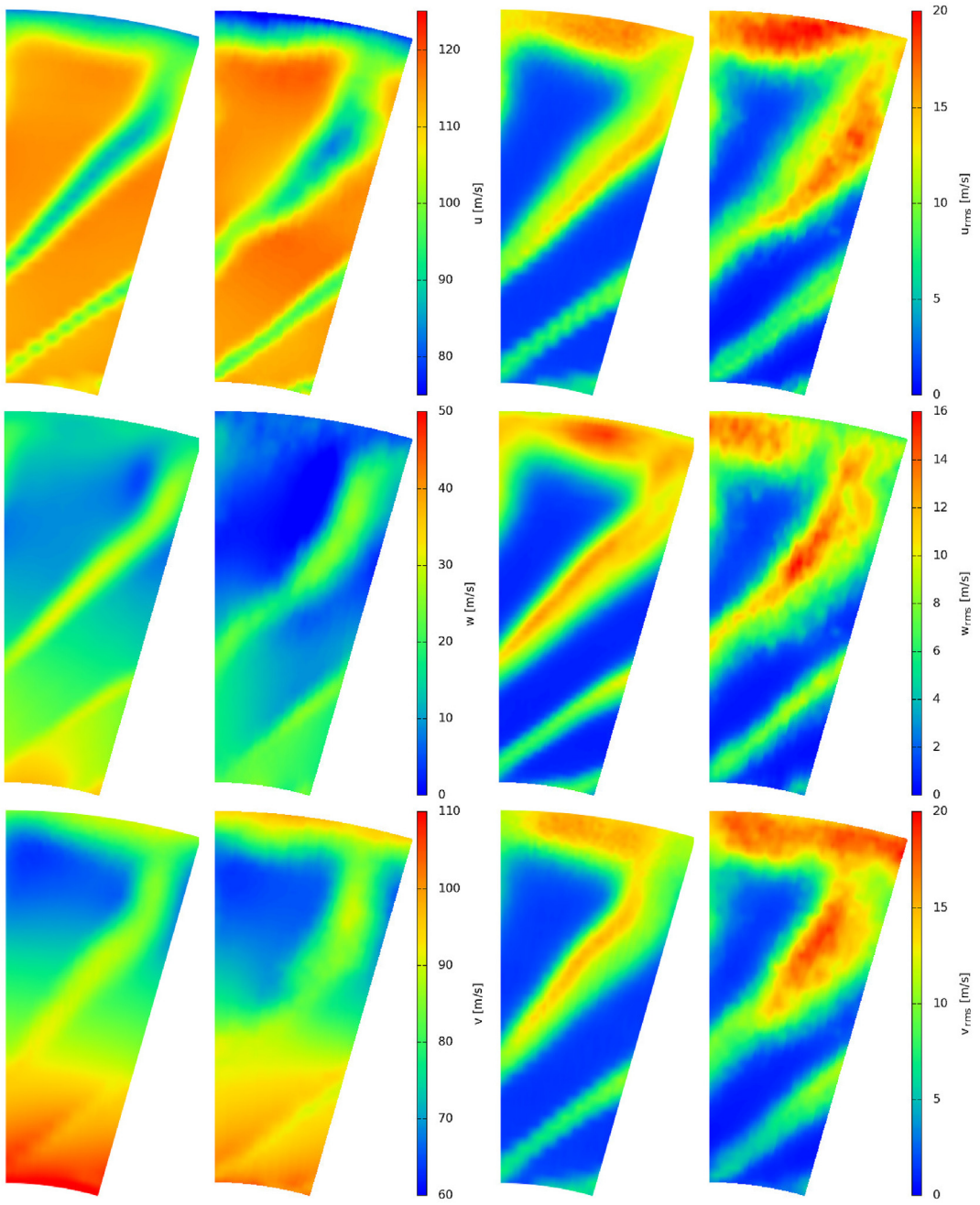

Fig. 5. Phase-locked average (left block) and SDV velocity (right block) at station #1 for the low-noise OGV [m/s]. Axial, radial and azimuthal velocity in the top, middle and bottom rows, respectively. Measurements on the left column, simulations on the right.

midpoint and an angle θ from the streamwise flow direction, reads:

$$S(r,\theta,\omega) = \left(\frac{\rho_\infty U_\infty \sin\theta}{2r}\right)^2 (kc)^2 \frac{L}{2} |\mathcal{L}|^2 \, l(\omega) \, S_v(\omega)\,, \tag{2}$$

where ρ_∞ and U_∞ are the free-stream density and velocity, $k = \omega/c_\infty$ is the acoustic wavenumber, ω is the radian frequency, c_∞ is the speed of sound, $\mathcal{L}$ is the aerofoil response function, l is the spanwise correlation length, and S_v is the PSD of the upwash velocity component. The Helmholtz number kc can be written as $U_\infty k_x c/c_\infty$, where $k_x = \omega/U_\infty$ is the streamwise wavenumber

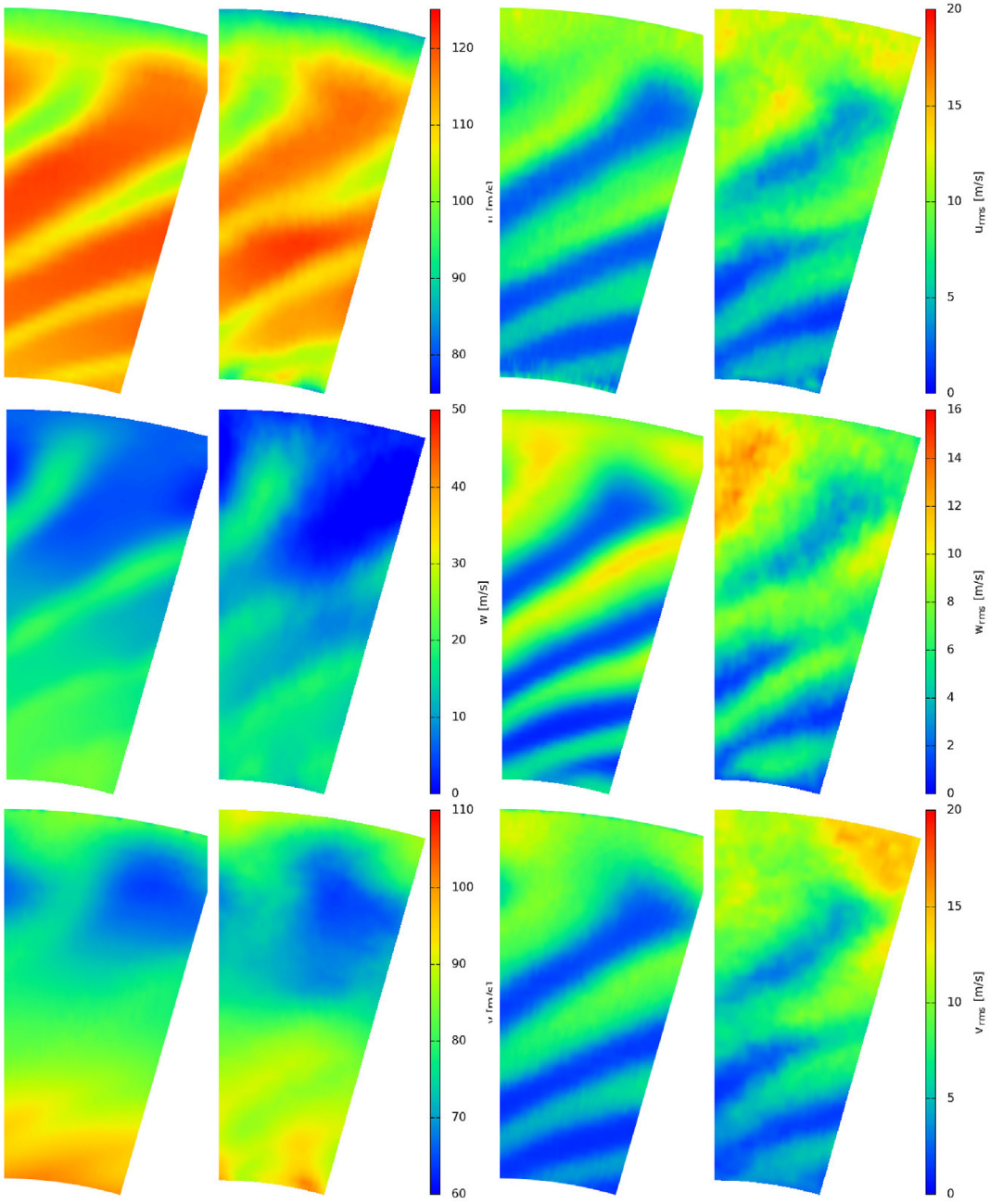

Fig. 6. Phase-locked average (left block) and SDV velocity (right block) at station #2 for the low-noise OGV $[\mathrm{m/s}]$. Axial, radial and azimuthal velocity in the top, middle and bottom rows, respectively. Measurements on the left column, simulations on the right.

of an impinging turbulent perturbation of frequency ω. Hence, the far-field noise PSD reads:

$$S(r,\theta,\omega) = \left(\frac{\rho_\infty U_\infty^2 k_x c \sin\theta}{2rc_\infty}\right)^2 \frac{L}{2}|\mathcal{L}|^2\, l(\omega)\, S_v(\omega)\,. \tag{3}$$

This expression reveals a U_∞^4 power-law of the far-field noise levels, and a quadratic proportionality to the magnitude of the Fourier component v of the upwash velocity fluctuation. The relative error of S in logarithmic scale can be thus evaluated as:

$$\delta S_{\mathrm{dB}} = 10\log\left(1 + 4\frac{\delta U_\infty}{U_\infty} + 2\frac{\delta v}{v}\right). \tag{4}$$

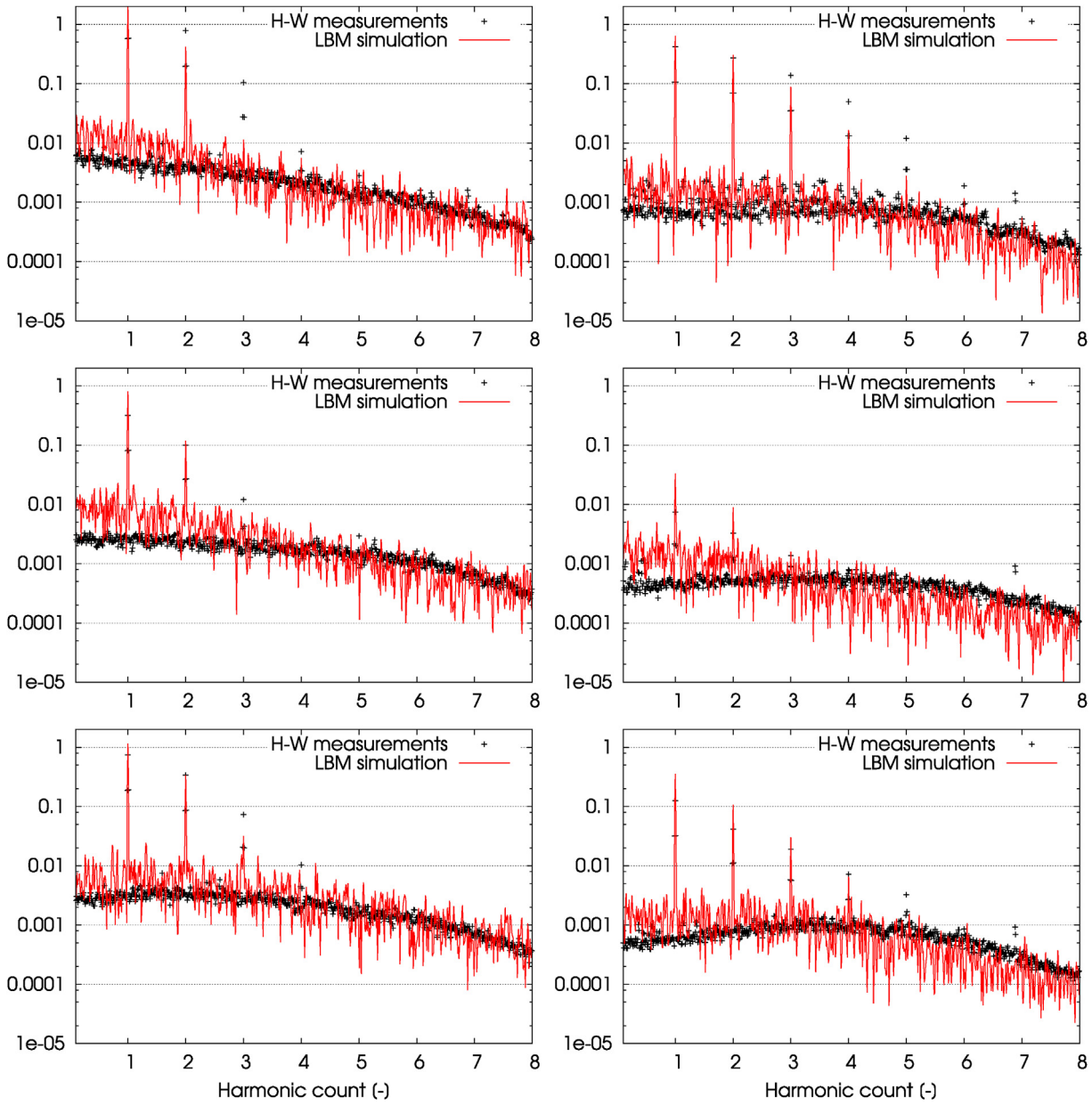

Fig. 7. Velocity spectra at station #1 for the baseline OGV. Axial, radial and azimuthal velocity on the top, center and bottom, respectively (in m/s). Comparison between H-W measurements (symbols) and PowerFLOW results at $r = 0.223292$ m ($r/R = 80.07\%$) on the left and $r = 0.167640$ m ($r/R = 60.11\%$) on the right.

From this expression, an error of 20% of the upwash velocity component results in an error of 1.46 dB of the far-field noise levels, which is in the order of the far-field noise measurements uncertainty of ± 1 dB.

A more quantitative comparison between measurements and simulation results can be performed by considering the velocity spectra at the same interstage locations. Fig. 7 shows, for the baseline configuration, spectra of the three velocity components plotted as a function of the harmonic count at about 80% and 60% of the casing-relative radial location. The comparison is quite satisfactory, both in terms of tonal and broadband levels. Better comparisons, in particular for the tonal components, are expected by covering a longer transient time.

Figs. 8 and 9 show comparisons between H-W measurements and simulation results at stations #1 and #2, respectively, for the low-noise configuration. As for the baseline configuration, the agreement is quite satisfactory, at both stations, both in terms of broadband and tonal levels.

The analysis of the unsteady velocity field in the interstage volume has shown that the accuracy of the numerical results is quite well preserved along the whole path of the rotor wake. This is a necessary but not sufficient condition to predict accurate

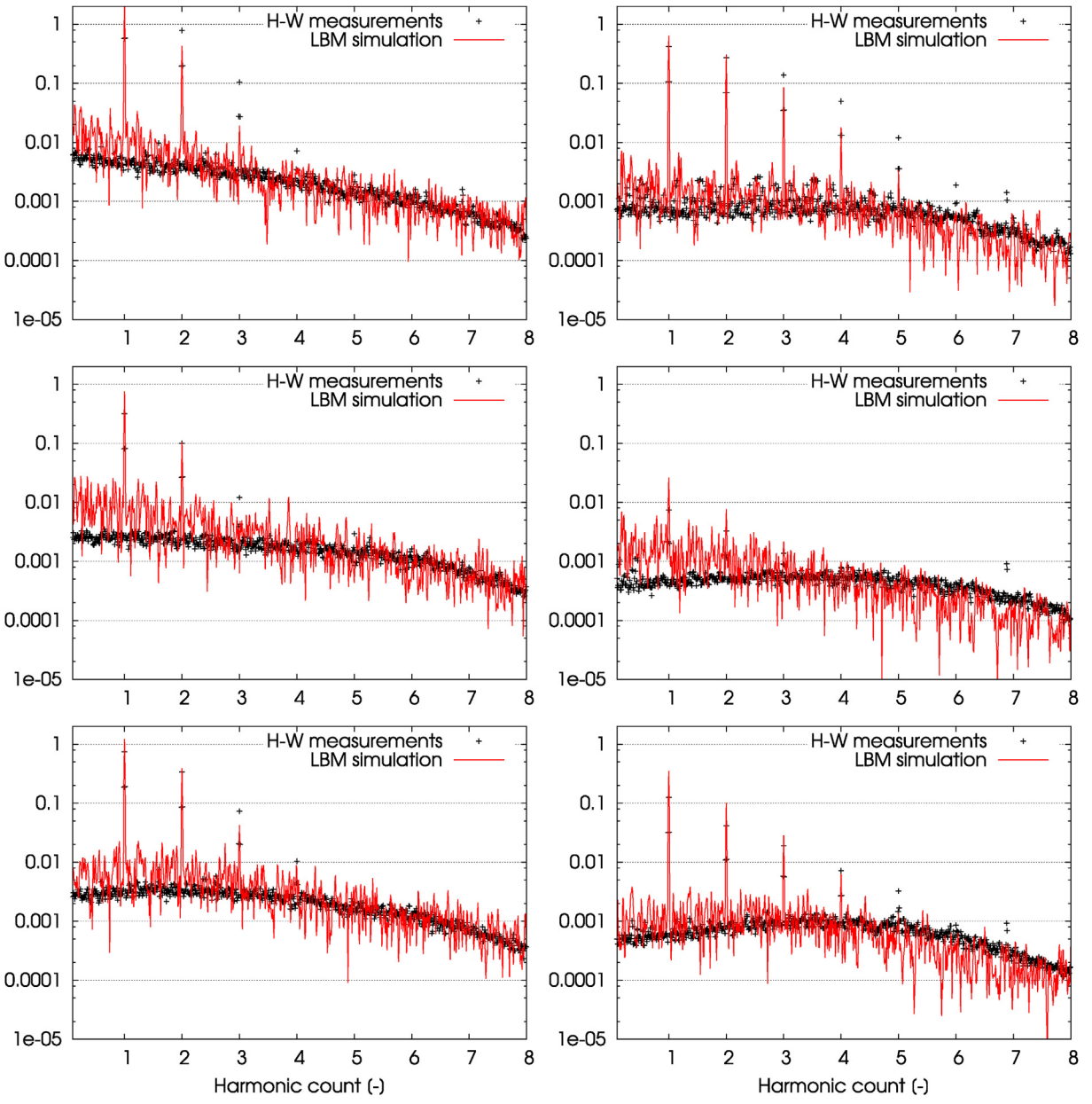

Fig. 8. Velocity spectra at station #1 for the low-noise OGV. Axial, radial and azimuthal velocity on the top, center and bottom, respectively (in m/s). Comparison between H-W measurements (symbols) and PowerFLOW results at $r = 0.223292$ m ($r/R = 80.07\%$) on the left and $r = 0.167640$ m ($r/R = 60.11\%$) on the right.

absolute and relative rotor/stator interaction noise levels, and therefore capture the effects of OGV modifications on the radiated noise. As relevant to the present study, Fig. 10 shows the comparisons between measurements and predictions in terms of differences between the baseline configuration and the other two configurations. Two quantities are considered: the overall sound pressure level (OASPL) at microphone located on a linear sideline array, 2.25044 m away from the engine axis, with a constant angular spacing of 5° from 30° to 140°, and the sound power level (PWL) computed by integration of the far-field acoustic intensity over a spherical surface portion corresponding to a circular array of 10 m radius, with a constant angular spacing of 5°, extending from 30° (front) to 150°. The agreement for both quantities is very good, being within the experimental uncertainty of ± 1 dB.

From the analysis of the reference SDT results, it could be argued that the employed computational methodology can provide reliable indications about possible noise reduction trends associated with the usage of wavy OGVs.

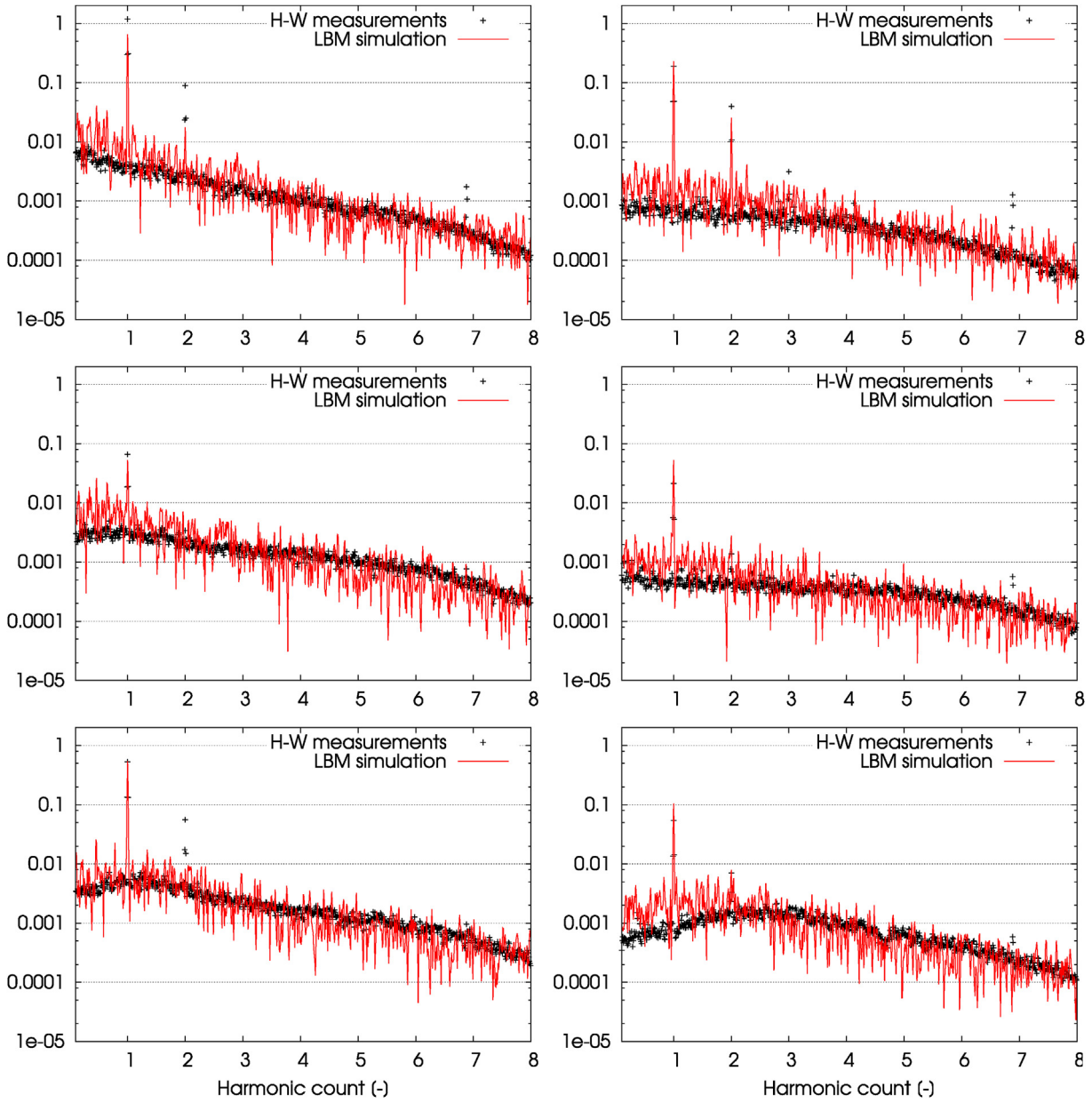

Fig. 9. Velocity spectra at station #2 for the low-noise OGV. Axial, radial and azimuthal velocity on the top, center and bottom, respectively (in m/s). Comparison between H-W measurements (symbols) and PowerFLOW results at $r = 0.223292$ m ($r/R = 80.07\%$) on the left and $r = 0.167640$ m ($r/R = 60.11\%$) on the right.

5. Integral scales of turbulence impinging on the OGV

Similarly to a wing section in a turbulent flow, the acoustic effectiveness of an OGV leading edge serration is expected to depend on ratios between the integral scales of the turbulent fluctuations in the impinging rotor wake and the amplitude and wavelength of the undulation. As shown by Gea-Aguilera et al. [14] for cases of impinging anisotropy turbulence, the maximum noise reduction can be achieved when the integral scale of the chordwise velocity component along the chordwise direction is smaller than the peak-to-valley serration distance ($L_x < 2h_s$) and the integral scale of the spanwise velocity component in the spanwise direction is smaller than the undulation wavelength ($L_z \lesssim \lambda_s/2$).

The turbulence in the rotor wake is herein characterized in terms of its integral length scale (L_{ij}) along the streamwise (x), radial (r) and azimuthal (θ) directions. They are estimated by using the fluctuations of the velocity components obtained removing the phase-locked average. The integral length scales of the resulting turbulence velocity fluctuations are then computed following the statistical approach proposed by Gea-Aguilera et al. [14] and further verified by using the magnitude-square-

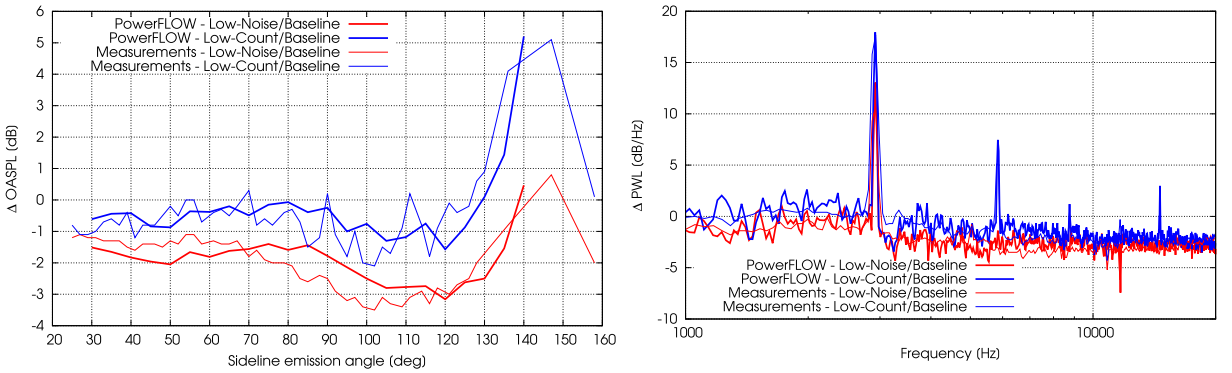

Fig. 10. Relative far-field OASPL along the sideline array (left) and PWL (right).

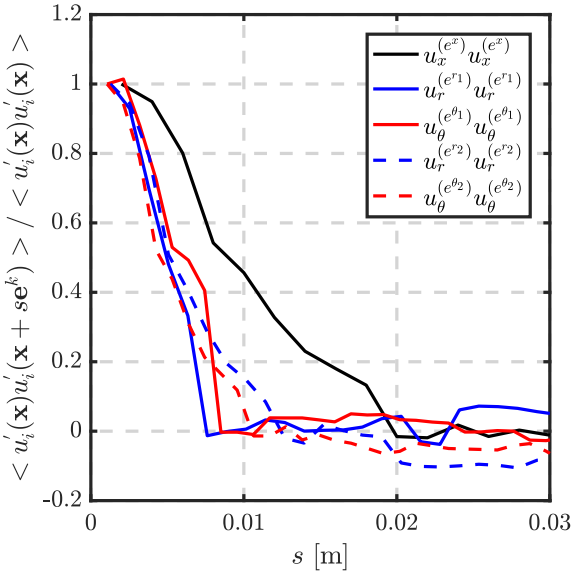

Fig. 11. Non-dimensional cross-correlation of the velocity fluctuations as in Eq. (5).

coherence approach used, among several others, by Avallone et al. [27]. The former estimates L_{ij}^k in the direction k as:

$$L_{ij}^k(\mathbf{x}) = \int_0^\infty \frac{\left\langle u_i'\left(\mathbf{x}+s\mathbf{e}^k\right) u_j'(\mathbf{x})\right\rangle}{\left\langle u_i'(\mathbf{x})\, u_j'(\mathbf{x})\right\rangle} \mathrm{d}s, \tag{5}$$

where $\mathbf{e}^k$ is the unitary vector in the kth direction, $\langle\cdot\rangle$ is the ensemble average, and s is the separation distance. In order to estimate the integral length scale of turbulent fluctuations in different frequency bands, the two-point coherence between different velocity components is computed and used to calculate the following integral scales:

$$L_{ij}^k(\mathbf{x}, f) = \int_0^\infty \gamma_{ij}\left(f, \mathbf{x}, \mathbf{x}+s\mathbf{e}^k\right) \mathrm{d}s, \tag{6}$$

where

$$\gamma_{ij}^2\left(f, \mathbf{x}, \mathbf{x}+s\mathbf{e}^k\right) = \frac{\left|\phi_{u_i u_j}\left(f, \mathbf{x}, \mathbf{x}+s\mathbf{e}^k\right)\right|^2}{\phi_{u_i u_i}(f, \mathbf{x})\, \phi_{u_j u_j}\left(f, \mathbf{x}+s\mathbf{e}^k\right)}, \tag{7}$$

is the coherence square and $\phi_{u_i u_j}$ is the cross-spectral density of the two velocity components u_i' and u_j'. Due to the non-homogeneity of the turbulent flow in the wake of the rotor, usage of this expression can lead to wrong estimates of the integral scales. This risk can be reduced by comparing the length scales computed at different points, and by using the phase-locked

Table 2
Integral scales of turbulent velocity fluctuations in the SDT engine interstage.

Integral length	Value (mm)
$L^{x}_{u_1 u}$	6.5
$L^{r_1}_{v_r v_r}$	6.8
$L^{\theta_1}_{v_\theta v_\theta}$	4.5
$L^{r_2}_{v_r v_r}$	6.5
$L^{\theta_2}_{v_\theta v_\theta}$	4.0

average removed velocity to compute the cross-spectrum in Eq. (7). This procedure should provide length scales that can be interpreted in relation with the canonical problem of an aerofoil in a homogeneous turbulent field.

The correlations are computed between signals extracted along five lines from a volume transient solution file sampled at the frequency of 458 kHz and covering one blade passage from the rotor to the stator. These lines, oriented in the azimuthal, radial and streamwise directions, form two crosses that share the same axial line. They are extracted at two reference points with centres at about 80% of the passage, and two axial locations, the first one at $x = 0.18$ m (5 mm upstream of the baseline OGV), and the second one at $x = 0.15$ m, where the origin of the reference system being located in the midpoint of the rotor. The two pairs of radial and azimuthal extraction directions are denoted as (e_{r_1}, e_{θ_1}) and (e_{r_2}, e_{θ_2}), respectively. The solution is also extracted along the axial direction e_x connecting the two points. The non-dimensional cross-correlation of the different velocity components is plotted in Fig. 11, and the corresponding integral scales are reported in Table 2. The integral scales along the radial and azimuthal directions are slightly larger at the location closer to the OGV in line with the measurements made by Podboy et al. [28] who evaluated the integral scales at the two axial locations, say the H-W stations #1 and #2 introduced in section 3, and reported integral scales that increase farther downstream of the rotor. Furthermore, as shown by Grace et al. [29], the integral scale along the azimuthal direction is slightly smaller than along the other directions.

On the base of these results, only the baseline OGV designs #5 and #6 are expected to satisfy both the axial and radial criteria for noise reduction, although only marginally for designs #5. It is indeed worth mentioning that, as shown by Maunus et al. [30] and Grace et al. [29], all the integral scales increase monotonically along the radial direction. Therefore, since the correlations have been computed at about 80% of the interstage radial passage, it is reasonable to expect that, for the radial OGV design #5, the axial integral satisfies the condition $L_x \lesssim 2h_s$ over a certain passage percentage. Whereas, the condition should be satisfied along the whole radial passage for design #6. Conversely, this is likely not the case for the swept OGV design #3, because of its larger distance from the rotor and the expected increasing scales farther downstream of the rotor, as observed experimentally for the SDT fan stage by Podboy et al. [28].

Finally, Fig. 12 shows the frequency-dependent integral scales. Consistently with the previous estimations, the axial integral scale is higher than in the other directions and below the threshold values of about 7 mm in both the axial and radial directions for the baseline OGV designs # 5. An interesting property of these results is that, after a rapid drop below about 2–3 kHz, the

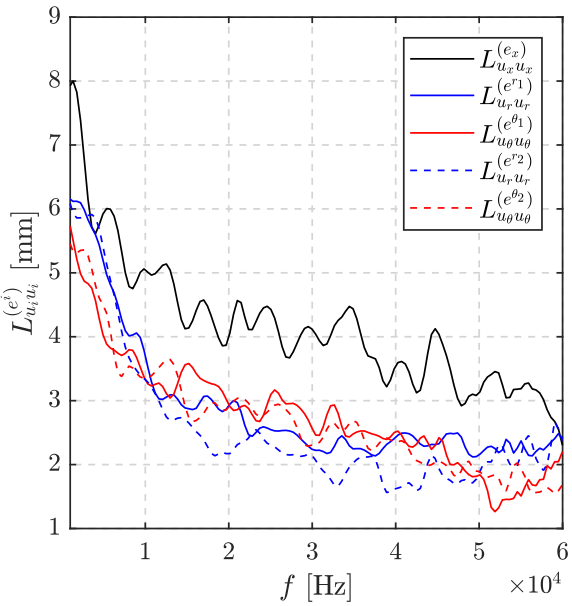

Fig. 12. Frequency-dependent integral scales as in Eq. (6).

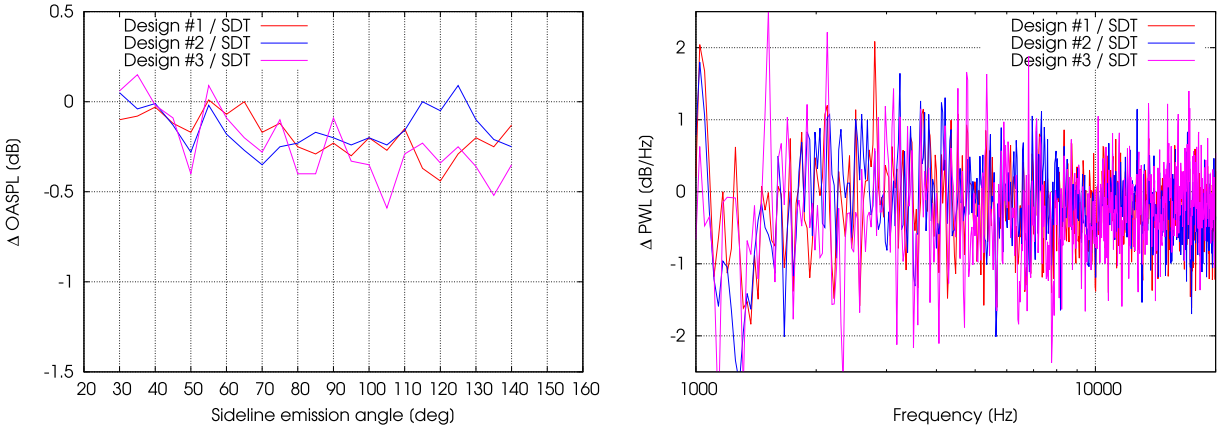

Fig. 13. Effect of different leading-edge serrations for the low-noise configuration (designs #1–#3). Relative far-field OASPL along the sideline array (left) and PWL (right).

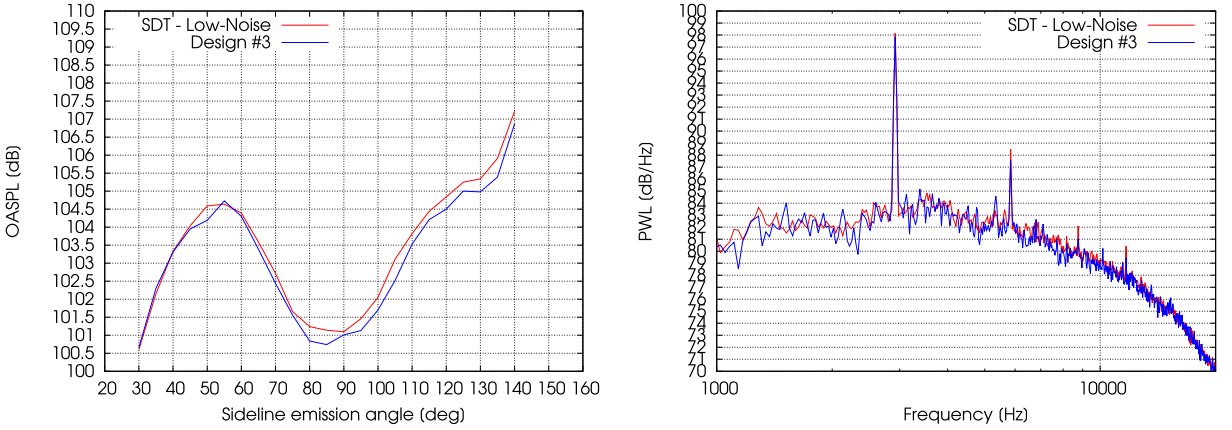

Fig. 14. Effect of leading-edge serration for the low-noise configuration (designs #3). Far-field OASPL along the sideline array (left) and PWL (right).

integral scales decay very slowly with frequency. It is therefore expected that, in agreement with the experimental observation made by Chaitanya et al. [9], if the serration amplitude and wavelength are large enough compared to the overall integral scales, the noise reduction should have a broadband character, with a slowly increasing trend above a certain frequency threshold.

6. Effects of serrations

Three serration designs are initially considered for the Low-Noise OGV (Table 1). According to the estimated integral scales of the interstage turbulence at a location close to the leading edge of the baseline OGV, non of them has the potential to reduce the noise. Successively, three serration designs are considered for the baseline OGV, and two of them (designs #5 and #6) are expected to satisfy the criteria for the integral scales, thus resulting in some significant noise reduction. The results are reported in this section in their chronological order.

Fig. 13 shows differences in terms of far-field OASPL and noise PWL for the three serrated low-noise OGVs. Far-field noise reductions up to 0.5 dB can be observed, with slightly better performances for designs #1 and #3. This confirms that the undulation amplitude for design #2 is too small compared to the integral scales of the impinging fluctuations, both in the axial and radial directions. However, all the achieved noise reductions are too small and likely in the order of the statistical convergence error of the simulations. The PWL differences exhibit a large spectral variance around 1 dB and it is hard to identify a clear noise reduction trend, as well as a clear difference between the three designs. Both the axial and radial integral scales are indeed too large compared to the root-to-peak distance and semi-wavelength of the serrations, thus resulting in no significant noise reduction.

Fig. 14 shows absolute far-field OASPL and noise PWL for the reference Low-Noise OGV and the serrated edge design #3. The only visible effect in the PWL spectrum is a 1 dB reduction of the BPF2 peak.

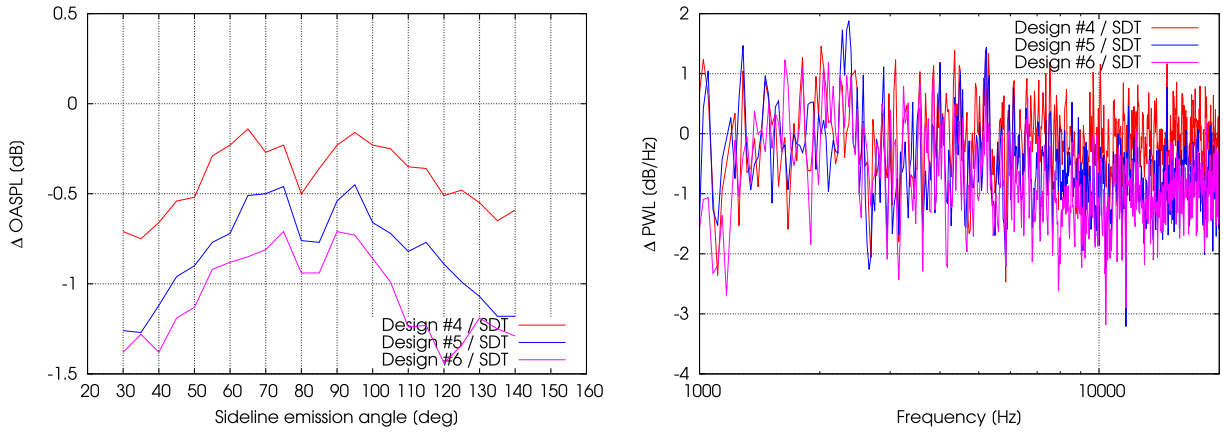

Fig. 15. Effect of different leading edge serrations for the baseline configuration (designs #4-#6). Relative far-field OASPL along the sideline array (left) and PWL (right).

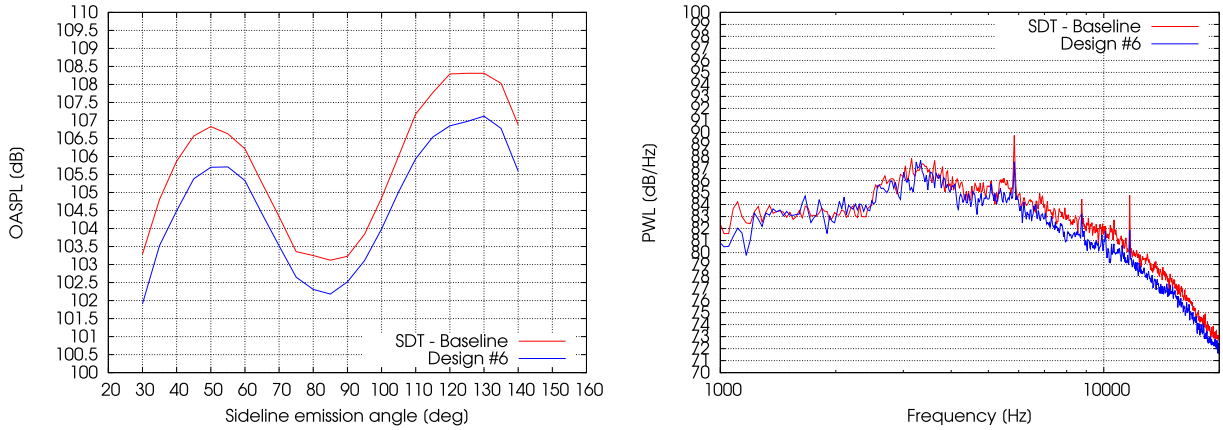

Fig. 16. Effect of leading edge serration for the baseline configuration (design #6). Far-field OASPL along the sideline array (left) and PWL (right).

Fig. 15 shows differences in terms of far-field OASPL and noise PWL for the serrated baseline OGV. Far-field noise reductions between 0.2 dB and 0.75 dB have been predicted for design #4, between 0.5 dB and 1.25 dB for design #5, and between 0.75 and 1.5 for design #6. The PWL spectra exhibit a clear noise reduction trend for the three designs starting from about 2 to 3 kHz. In agreement with the integral scale geometric criteria, design #6 is more efficient than designs #3 and #4. Very interestingly, the far-field OASPL exhibits the same noise reduction directivity patterns.

Finally, Fig. 16 shows absolute far-field OASPL and noise PWL for the reference Baseline OGV and the serrated edge design #6. In this case, the PWL shows some broadband noise reduction starting from a frequency of about 3 kHz, and a net reduction trend above 6 kHz. The latter value corresponds to a Strouhal number fh_s/U of about 0.2, the average axial velocity U being about 110 m/s at a distance of 5 mm from the leading edge. Interestingly, Chaitanya et al. [9], determined a threshold Strouhal number of 0.2 also for the case of an aerofoil in isotropic turbulence. Further simulations are required in order to confirm the generality of this result.

7. Flow visualization

Turbulent structures in the rotor wake impinging on the serrated Baseline OGV (design #6) are shown in Fig. 17 using the Lambda2 vortex criterion [31]. A transient volume measurement covering one blade passage from the rotor to the stator is used. The number of vanes encompassed by this volume is thus equal to about 2.45. Two frames separated by $2.6 \cdot 10^{-5}$ s are considered to visualize the kinematics of some eddies impinging on the serration. Consistently with the phase-locked SDV velocity maps shown in Fig. 4, a higher level of turbulent activity can be observed in the tip region of the OGV. This is a consequence of the higher tangential velocity induced by the rotation of the fan, and of the presence of a turbulent boundary layer on the casing. Similarly to the interstage plane extractions shown in Fig. 4, the wake from the rotor appears to be split in two/three branches with regions of lower turbulence activity between them (void volumes).

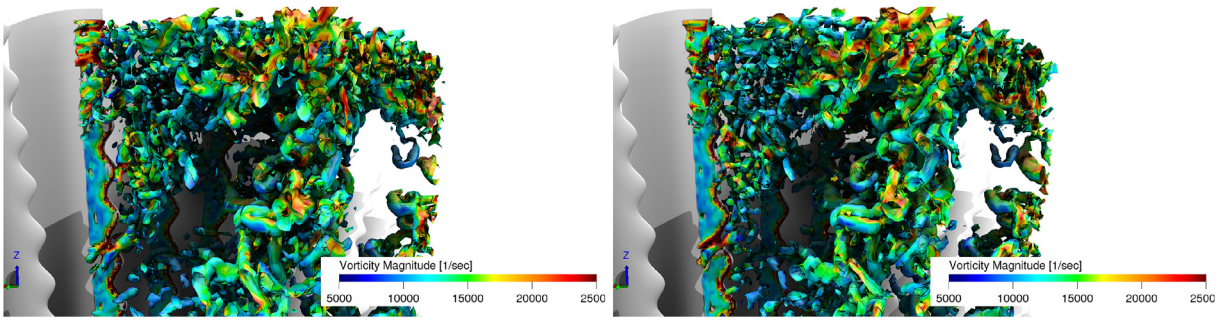

Fig. 17. OGV design #6: iso-surfaces $\lambda_2 = -2 \cdot 10^{-7}\ s^{-2}$ colored by velocity magnitude.

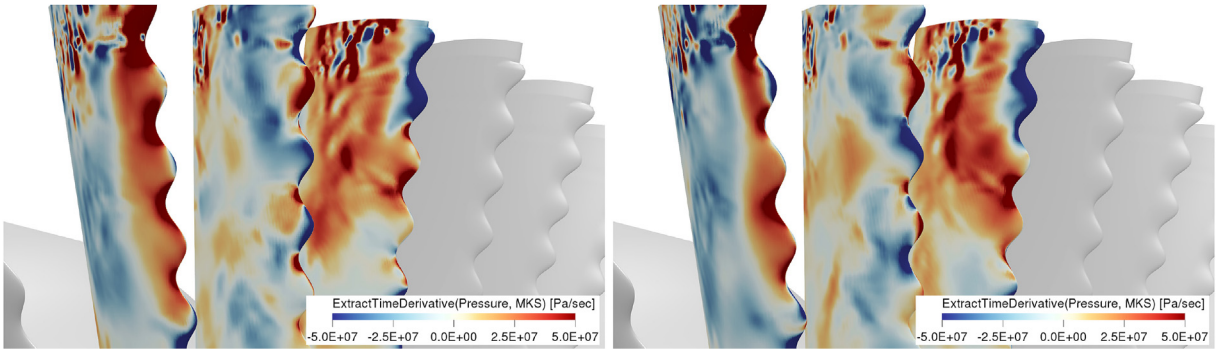

Fig. 18. OGV design #6: wall pressure time derivative.

Fig. 18 shows two snapshots of the wall pressure time derivative over about 45% of the vane span. Being proportional to the dilatation field, the wall pressure time derivative is a suitable quantity for noise source visualization. Both views shows the presence of higher turbulent fluctuations in the tip region. Two arbitrary frames are considered to highlight the occurrence of both peak-to-valley and peak-to-peak destructive interference taking place when the turbulent eddies impinge on the serration. More precisely, a peak-to-valley and a peak-to-peak phase opposition can be observed on the second vane from the left in the first and second snapshot, respectively. Due to the random nature of this flow/structure interaction process, it is hard to isolate flow patterns that reappear cyclically. Moreover, better than single frames, the animated pressure field reveal the higher level of noise generation in the tip region, as well as other interesting phenomena like the noise radiation from the OGV trailing edge. It can be therefore argued that a further improvement of the leading edge serration concept should take into account the effective radial distribution of the noise sources.

8. Conclusions

Different designs of serrated OGV leading edges have been simulated using a validated CFD/CAA solver based on the LB-VLES method. The NASA SDT engine geometry has been considered as a reference. Serrations have been applied both to a radial and a swept stator. In the explored design space, which is indeed limited to six different serration designs, no significant noise reduction has been observed, with the exception of two designs for the radial OGV, for which the serration peak-to-valley distance and spanwise wavelength were sufficiently large compared to the integral scales of the impinging turbulent fluctuations. More precisely, average noise reductions along the sideline microphone array of about 1 dB and 0.2 dB for the radial and swept OGVs have been obtained, respectively. The second value is below the numerical and experimental accuracy, thus revealing the usefulness of the leading-edge serration to reduce the noise of the low-noise OGV. Although the explored design space is rather small, the present results seem to confirm previous literature observations, both in terms of scale thresholds, say peak-to-valley distance larger than the axial integral scale and the half-wavelength smaller equal to or slightly larger than the radial integral scale, and the 0.2 Strouhal number threshold. Additional designs will be explored in the future in order to achieve more definitive conclusions about the interest of a wavy leading edge for rotor/stator interaction noise reduction. The analysis will be also extended to different engine configurations, like a modern ultra-high-bypass-ratio engine, and higher power operating conditions.

Acknowledgments

The authors wish to acknowledge Dr. Edmane Envia from NASA Glenn Research Center for providing the geometry and experimental data of the NASA 22-in fan source diagnostic test.

Appendix A. Supplementary data

Supplementary data to this article can be found online at https://doi.org/10.1016/j.jsv.2018.10.057.

References

[1] B. Owen, D.S. Lee, L. Lim, Flying into the future: aviation emissions scenarios to 2050, Environ. Sci. Technol. 44 (7) (2010) 2255–2260.
[2] P.T. Soderman, Aerodynamic Effects of Leading-edge Serrations on a Two-dimensional Irfoil, NASA TM 2008-2154115.
[3] F.G. Collins, Boundary layer control on wings using sound and leading edge serrations, AIAA J. 19 (2) (1981) 129–130.
[4] D.S. Miklosovic, M.M. Murray, L.E. Howle, Experimental evaluation of sinusoidal leading edges, AIAA J. Aircraft 44 (4) (2007) 1404–1408.
[5] D.S. Miklosovic, M.M. Murray, L.E. Howle, F.E. Fish, Leading-edge tubercles delay stall on humpback whale (megaptera novaeangliae) flippers, Phys. Fluids 16(5).
[6] M.J. Stanway, Hydrodynamic Effects of Leading-edge Tubercles on Control Surfaces and in Flapping Foil Propulsion. (Ph.D. thesis), Massachusetts Institute of Technology, Cambridge, MA, 2008.
[7] R.R. Graham, The silent flight of owls, J. Royal Aeronaut. Soc. 38 (1934) 837–843.
[8] G.M. Lilley, A Study of the Silent Flight of the Owl, AIAA Paper 1998-2340.
[9] P. Chaitanya, P. Joseph, S. Narayanan, C. Vanderwel, J. Turner, J.W. Kim, B. Ganapathisubramani, Performance and mechanism of sinusoidal leading edge serrations for the reduction of turbulence-aerofoil interaction noise, J. Fluid Mech. 818 (2017) 435–464.
[10] A.S.H. Lau, S. Haeri, J.W. Kim, The effect of wavy leading edges on aerofoil-gust interaction noise, J. Sound Vib. 332 (24) (2013) 6234–6253.
[11] V. Clair, C. Polacsek, T.L. Garrec, G. Reboul, M. Gruber, P. Joseph, Experimental and numerical investigation of turbulence-airfoil noise reduction using wavy edges, AIAA J. 51 (11) (2013) 2695–2713.
[12] J.W. Kim, S. Haeri, P. Joseph, On the reduction of aerofoil-turbulence interaction noise associated with wavy leading edges, J. Fluid Mech. 792 (2016) 526–552.
[13] M. Roger, C. Schram, L.D. Santana, Reduction of Airfoil Turbulence-impingement Noise by Means of Leading-edge Serrations And/or Porous Materials, AIAA Paper 2013–2108.
[14] F. Gea-Aguilera, J.R. Gill, D. Angland, X. Zhang, Wavy Leading Edge Airfoils Interacting with Anisotropic Turbulence, AIAA Paper 2017-3370.
[15] R.P. Woodward, C. Hughes, R. Jeracki, C. Miller, Fan Noise Source Diagnostic Test-farfield Acoustic Results, AIAA Paper 2002-2427.
[16] E. Envia, Fan Noise Source Diagnostic Test-vane Unsteady Pressure Results, AIAA Paper 2002-2430.
[17] D. Casalino, A. Hazir, A. Mann, Turbofan broadband noise prediction using the lattice Boltzmann method, AIAA J. 56 (2) (2018), https://doi.org/10.2514/1.J055674.
[18] X. Shan, X.-F. Yuan, H. Chen, Kinetic theory representation of hydrodynamics: a way beyond the Navier-Stokes equation, J. Fluid Mech. 550 (2006) 413–441.
[19] X. Nie, X. Shan, H. Chen, A Lattice-boltzmann/finite-difference Hybrid Simulation of Transonic Flow, AIAA Paper 2009-0139.
[20] H. Chen, S. Chen, W. Matthaeus, Recovery of the Navier-Stokes equations using a lattice-gas Boltzmann method, Phys. Rev. A 45 (8) (1992) 5339–5342.
[21] V. Yakhot, S.A. Orszag, Renormalization group analysis of turbulence. i. basic theory, J. Sci. Comput. 1 (1) (1986) 3–51.
[22] H. Chen, C. Teixeira, K. Molvig, Realization of fluid boundary conditions via discrete Boltzmann dynamics, Int. J. Mod. Phys. C 9 (8) (1998) 1281–1292.
[23] D. Casalino, An advanced time approach for acoustic analogy predictions, J. Sound Vib. 261 (4) (2003) 583–612.
[24] F. Farassat, G.P. Succi, The prediction of helicopter discrete frequency noise, Vertica 7 (4) (1983) 309–320.
[25] A. Najafi-Yazdi, G.A. Brès, L. Mongeau, An acoustic analogy formulation for moving sources in uniformly moving media, Proc. Roy. Soc. Lond. A 467 (2125) (2011) 144–165.
[26] R.K. Amiet, Acoustic radiation from an airfoil in a turbulent stream, J. Sound Vib. 41 (4) (1975) 407–420.
[27] F. Avallone, S. Pröbsting, D. Ragni, Three-dimensional flow field over a trailing-edge serration and implications on broadband noise, Phys. Fluids 28 (11).
[28] G.C. Podboy, M.J. Krupar, S.M. Helland, C.H. Hughes, Steady and Unsteady Flow Field Measurements within a Nasa 22-inch Fan Model, AIAA Paper 2002-1033.
[29] S.M. Grace, A. Gupta, I.G. Martino, D. Casalino, Statistics and Structure of Turbulence in Fan/fegv Interstage and Their Aeroacoustic Implications, AIAA Paper 2018-4186.
[30] J. Maunus, S.M. Grace, D.L. Sondak, V. Yakhot, Characteristics of turbulence in a turbofan stage, J. Turbomach. 135(2).
[31] J. Jeong, F. Hussain, On the identification of a vortex, J. Fluid Mech. 285 (1995) 69–94.